Earth and Planetary Science Letters 299 (2010) 263–272

Contents lists available at ScienceDirect

Earth and Planetary Science Letters

journal homepage: www.elsevier.com/locate/epsl

Ozone perturbation from medium-size asteroid impacts in the ocean

E. Pierazzo [a,*], R.R. Garcia [b], D.E. Kinnison [b], D.R. Marsh [b], J. Lee-Taylor [b], P.J. Crutzen [c]

[a] Planetary Science Institute, 1700 E. Ft. Lowell Rd., Suite 106, Tucson AZ 85719, USA
[b] National Center for Atmospheric Research, P.O Box 3000, Boulder, CO 80307-3000, USA
[c] Max-Planck Institut for Chemistry, Division of Atmospheric Chemistry. P.O. Box 3060. D-55020 Mainz, Germany

ARTICLE INFO

Article history:
Received 3 June 2010
Received in revised form 24 August 2010
Accepted 31 August 2010
Available online 17 October 2010

Editor: L. Stixrude

Keywords:
oceanic impact
Near-Earth-Object
modeling
ozone perturbation
atmospheric chemistry

ABSTRACT

We present results of an investigation aimed at characterizing the effects of oceanic impacts of 500 m and 1 km diameter asteroids on the lower and middle atmosphere, estimating ozone loss and potential danger from UV radiation at the Earth's surface. Little work has been done so far to assess the atmospheric perturbation from the impact of objects in this size range, even though their sizes are close to the threshold for causing global environmental effects. In particular, at the Earth's surface oceanic impacts are twice more likely to occur than land impacts. This work represents the first attempt at combining impact simulations with a three-dimensional shock physics code (SOVA), and atmospheric simulations using the general circulation model with interactive chemistry WACCM. SOVA simulations provided an estimate of the amount and state of material ejected into the atmosphere by the impacts. Estimated water vapor in the upper atmosphere was then introduced in the initial conditions for the WACCM simulations that modeled the subsequent perturbation of atmospheric chemistry Final estimates of the change over time in UV flux at the surface due to the impact-induced ozone change are then carried out using the TUV radiative transfer model. The results suggest that mid-latitude oceanic impacts of 1 km asteroids can produce a significant, global perturbation of upper atmospheric chemistry, including multi-year global ozone depletion comparable to ozone hole records registered in the mid-1990 s. Asteroids 500 m in diameter cause limited perturbations of upper atmospheric chemistry with significant ozone depletion confined to the hemisphere in which the impact occurred. Impact-induced ozone depletion affects UV irradiance at the Earth's surface, resulting in levels of UV-B irradiance that can be dangerous for living organisms, and, in the tropics and initial midlatitude summers, far exceed levels currently experienced anywhere on Earth.

1. Introduction

Awareness of the devastating consequences of impact events on the fragile terrestrial ecosystem arose in the 1980 s with the revolutionary theory of Alvarez et al. (1980) linking the great end-Cretaceous mass extinction to an asteroid impact (see Schulte et al., 2010). This led to the development in the early 1990 s of the Spaceguard Survey, with the goal of identifying 90% of all Near-Earth Objects (NEOs) larger than 1 km in diameter by 2008 (Pilcher, 1998). These asteroids are believed to be large enough to potentially cause a global climate disaster and destroy human civilization (Chapman and Morrison, 1994). The last 10% of these large NEOs includes objects that may be more difficult to observe due to various factors (very low albedo, very high inclinations, orbits too close to the Sun). The official NASA NEOs website (http://neo.jpl.nasa.gov/stats/) indicates that, as of Sep 2010, the number of discovered NEOs >1 km was 817. Estimates of the total population of large NEOs depend on the models used to determine the evolution of the asteroid population. Harris (2008) estimates a population of 940, close to the 960 estimated by Bottke et al. (2002), suggesting that approximately 85% of NEOs >1 km have been discovered. A slightly higher estimate by Stokes et al. (2003) of up to 1100 large NEOs corresponds to a significantly lower percentage of discovered NEOs, about 74%. Overall, there is high confidence that all asteroids ≥10 km in diameter have been discovered and tracked, significantly decreasing (at least for the near future) the hazard of a major mass extinction impact event (Harris, 2008). The objects discovered so far have a very small probability of hitting Earth in the next 50 years or more, thus reducing the assessed "risk" of impact at least in the short term. Still, it appears that well over a hundred objects 1 to 2 km in diameter are currently looming undiscovered in the Earth's neighborhood. Smaller and much more abundant NEOs in the size range between about 300 m and 1 km in diameter are also believed to pose a significant threat to human civilization. The consequences of a collision of a NEO in this size range with the Earth have never been explored in detail.

Over 70% of the Earth's surface is covered by water, and about two-thirds is covered by oceans over 1 km deep. As a result, impacts into

* Corresponding author. Tel.: +1 520 547 3951; fax: +1 520 622 8060.
E-mail addresses: betty@psi.edu (E. Pierazzo), rgarcia@ucar.edu (R.R. Garcia), dkin@ucar.edu (D.E. Kinnison), marsh@ucar.edu (D.R. Marsh), julial@ucar.edu (J. Lee-Taylor), paul.crutzen@mpic.de (P.J. Crutzen).

0012-821X/$ – see front matter © 2010 Elsevier B.V. All rights reserved.
doi:10.1016/j.epsl.2010.08.036

oceans are twice more probable than land impacts. Much effort has been devoted lately to understanding the risk of impact-generated tsunami, but little work has been done so far to assess the atmospheric (and thus, climatic) effects of oceanic impacts of mid-size bolides. Recently, Birks et al. (2007) investigated the effects of large amounts of water delivered to the upper atmosphere in small to medium size (150 m to 1 km) asteroid impacts. After roughly estimating the amounts of nitrogen oxide produced by the bolide moving through the Earth's atmosphere and the water ejected by these impacts, they introduced these perturbations into a single latitude-longitude grid column (5°×5°) at altitudes above 70 km of the Thermosphere Ionosphere Mesosphere Electrodynamics General Circulation Model (TIME-GCM; Roble and Ridley, 1994), an upper atmosphere general circulation model coupled with an interactive chemistry package. They found that the injected water produces strong chemical perturbations in the upper atmosphere, quickly propagating to the middle and upper stratosphere, and causing upper atmosphere ozone depletion for months after the impact. They concluded that impactors around 500 m and larger would cause perturbations that may have serious effects on the biosphere. That study, however, could not characterize the perturbation of the atmosphere below about 30 km (the peak in ozone concentration occurs in the region of 20 to 30 km; Seinfeld and Pandis, 1998), nor could it calculate its impact on atmospheric chemistry of the chlorine or bromine families, two important ozone catalysts and important components of sea salt.

This paper presents initial results of an investigation aimed at characterizing the effects of medium-size oceanic impacts on the lower and middle atmosphere and estimating ozone loss and potential danger from UV radiation at the Earth's surface. The work combines a shock physics code, to evaluate the effects of impacts, and a state-of-the-art whole atmosphere general circulation model with an interactive chemistry model, to characterize the perturbation of atmospheric chemistry. Final estimates of the change over time in UV flux at the surface due to the modeled impact-induced ozone change over time are then carried out using a radiative transfer model.

2. Numerical models

The numerical simulations involve several phases, starting with the definition of the impact calculations, whose outputs are used as initial conditions for the atmospheric model, while the ozone column density calculated with the atmospheric model is used to estimate surface UV levels. These steps are described in detail below.

2.1. Impact simulations

We model asteroid impacts into a 4 km deep ocean with the 3D shock physics code SOVA (Shuvalov, 1999) coupled with tabular equations of state built from the ANEOS equation of state package (Thompson and Lauson, 1972). The simulations are carried out in a local, Cartesian grid (with the origin at the point of impact) and assume bilateral symmetry, which makes it possible to limit the model domain to the half space corresponding to $y>0$ ($y<0$ represents the mirror half space) starting from the impact plane (or symmetry plane), identified by the direction of impact and the perpendicular to the surface at the impact point, the z direction (downrange from the impact corresponds to $x>0$). The simulations started with a spatial resolution of 20 cells per projectile radius over a central region around the impact point to accurately resolve the initial propagation of the shock wave in the target. For SOVA this is a good compromise between the need for high resolution to resolve the shock wave and the need to reduce computing time by limiting the number of computational cells (Pierazzo et al., 2008). As the simulation covered several minutes after the impact, the mesh size boundaries were extended upward and outward over time to follow the expanding impact plume while increasing the size of individual cells.

Asteroids have densities around 2000 to 3000 kg/m^3 and reach the Earth's atmosphere with velocities in the range of 11 to 30 km/s. Root mean square velocities, quoted as characteristic impact velocities for NEOs, are about 20 km/s (e.g., Morrison et al., 2002); however, root mean square values tend to be skewed by small numbers of high impact velocity objects (Chyba, 1991). Estimates of impact velocities from a debiased population of NEOs larger than about 1 km (Bottke et al., 2002) suggests that about 50% of the impactors have impact velocities below 18–19 km/s, while the estimated mean impact velocity for that population is 20.3 km/s (Bottke, personal comm.). Higher impact velocities result in stronger shocks, increasing the amount of vaporized ocean water ejected in the impact. For the present simulations we adopt a characteristic impact velocity of 18 km/s. We modeled the impact of idealized spherical asteroids 500 m and 1 km in diameter, reaching the lower atmosphere at an impact angle of 45° from the surface (most probable angle of impact; e.g., Pierazzo and Melosh, 2000). Table 1 summarizes the impact parameters used in the simulations. The numerical model employed tabular versions of the ANEOS equation of state of granite ($\rho = 2630$ kg/m^3; Pierazzo et al., 1997), to model the impactor and the Earth's crust, and water (Turtle and Pierazzo, 2001) to model the ocean. A table for the standard atmosphere was used to represent the Earth's atmosphere.

To obtain accurate estimates of the shock state of water ejected on impact we distributed several hundred thousand Lagrangian tracers (massless particles that travel through the mesh with the velocity of the local material) in the ocean around the impact point. The fraction of water vaporized in the impact was estimated by determining the volume of ocean water shocked above about 20 GPa. This value is roughly half-way between the pressures for incipient vaporizaton, 5 GPa, and complete vaporization, 45 GPa, of water at room temperature calculated with ANEOS (Pierazzo et al., 1998). Fig. 1 shows the distribution of the tracers in the ocean around the impact point at the start of the simulation (upper panels) and in the atmosphere 9 minutes after the impact of an asteroid 1 km in diameter (lower panels). Different shock levels in the ocean water are displayed in different colors. The initial tracer distribution shows the shock intensity in the oceanic region (x–y and x–z planes) around the impact point. The distribution of tracers after 9 min shows the reach of water (liquid and vapor) ejected in the impact, which, for the 1 km asteroid impact, extends horizontally well over 1000 km, and vertically up to the thermosphere.

The impact simulations were extended over several minutes after the impact to record the expansion of ejected water into the upper atmosphere and the beginning of the collapse of the impact plume

Table 1
Parameters and variables associated with the small and large impact investigated in this study.

	Small impact	Large impact
Proj.: Diameter	0.5 km	1 km
Mass	1.721×10^{11} kg	1.377×10^{12} kg
Velocity	18 km/s	18 km/s
Angle	45°	45°
Energy	2.788×10^{19} J	2.23×10^{20} J
Material ejected above 15 km		
Max. projectile	8.37×10^{9} kg	2.33×10^{10} kg
Max. total water	4.41×10^{12} kg	4.18×10^{13} kg
Max. water vapor	1.1×10^{12} kg	1.2×10^{13} kg
Range of atmospheric perturbation*		
Ozone min–max (DU)	85.7 to 396.6	19.9 to 366.3
Ozone change min–max (%)**	−91.3 to 18.3	−68.3 to 18.1
UVI min–max	0 to 25.4	0 to 56.6

* Min-max of montly mean values evaluated over the duration of the simulations. For comparison, values for the unperturbed case are: *Ozone min-max*: 92 to 505 DU; *UVI min-max*: 0 to 18.

**Ozone change calculated from the unperturbed case: $100\times(perturb - unperturb)/unperturb$.

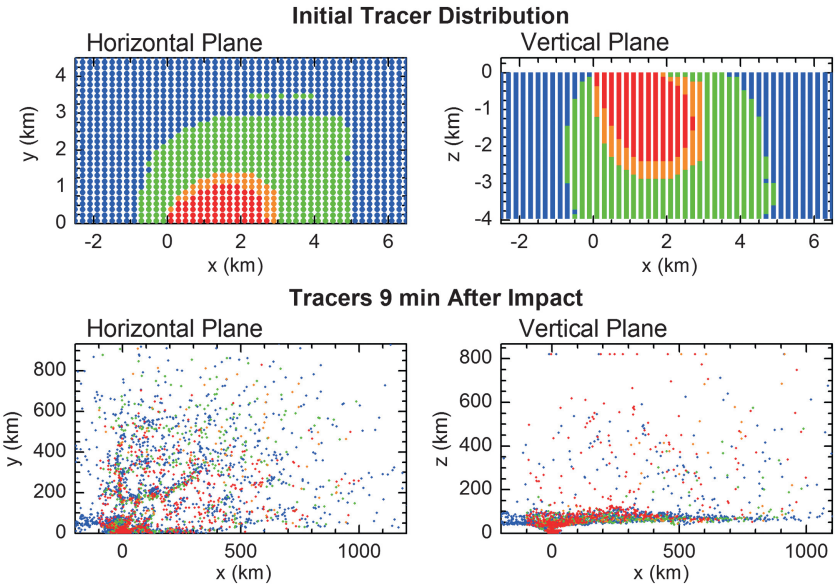

Fig. 1. Distribution of Lagrangian tracers used to estimate shock vaporization of ocean water in the 1 km asteroid impact at 18 km/s and 45°. Left: horizontal distribution (perpendicular to the plane of impact). Right: vertical distribution (parallel to the plane of impact). Blue dots: liquid water (P<5 GPa); green dots: water between incipient and 50% vaporization (5 GPa<P<20 GPa); Orange dots: water between 50% and complete vaporization (20 GPa<P<45 GPa); red dots: water vapor (P>45 GPa).

towards the lower atmosphere. Output/restart files provide the distribution of modeled materials within each cell of the mesh, as well as the location and peak shock pressure of the Lagrangian tracers at given timesteps (ranging from 1 s early in the simulation to 10 s at later stages). The distribution of water in the atmosphere over time, shown in Fig. 2, is then used to estimate the mass of water at various heights above the surface.

2.2. Atmospheric model

The effects of the impact on the chemistry and dynamics of the atmosphere were investigated using the Whole Atmosphere Community Climate Model (WACCM; Garcia et al., 2007; Kinnison et al., 2007), developed at the National Center for Atmospheric Research (NCAR). WACCM is a Chemistry-Climate Model based on the Community Atmosphere Model (CAM3, Collins et al., 2004) and extends from the Earth's surface through the lower thermosphere. It incorporates a complete physical mechanism that includes treatment of non-LTE (Local Thermodynamic Equilibrium) long-wave radiation and short-wave radiation in the far and extreme UV (ultraviolet) wavelengths, auroral processes, and ion drag and molecular diffusion above 65 km. Below 65 km, WACCM is similar to CAM3 (Collins et al., 2004), but with several important differences regarding gravity wave processes and vertical diffusion parameterizations, vertical resolution, and the position of the upper boundary. At all altitudes, WACCM incorporates a chemistry module (65 species) based on the Model of OZone And Related Tracers, version 3 (MOZART-3; Kinnison et al., 2007) and includes detailed descriptions of reactions and photolytic processes in the middle and upper atmospheres. Upper atmospheric processes are adapted from TIME/GCM (Roble and Ridley, 1994). Atmospheric dynamics and physics, and the interactive chemistry and physical parameterizations of the upper atmosphere are solved using 20-minute time steps via the finite volume scheme of Lin (2004) on a horizontal grid of 1.9°×2.5° (high resolution) or 4°×5° (low resolution) and a vertical domain of 66 levels extending from the ground to about 140 km (5.1×10−6 hPa). This version of WACCM has been run in support of the Chemistry-Climate Model Validation (CCMVal) project of SPARC (Stratospheric Processes and their Role in Climate), which is a research initiative sponsored by the World Climate Research Program. As such, the performance of the model has been thoroughly documented in reports and scientific investigations resulting from CCMVal (e.g., Eyring et al., 2006, 2010; SPARC CCMVal, 2010). Insofar as Chemistry-Climate Models are successful in simulating observed changes and trends in the atmosphere, it is possible to obtain insights into the mechanisms that produce the trends and to gain confidence that the code can be applied to prognostic simulation of the climate on decadal timescales, e.g., to study the recovery of ozone as atmospheric burden of halogenated gases decreases (see Eyring et al., 2007; Garcia et al., 2007).

The simulations covered a few years after impact, to record the duration of the post-impact perturbation and the recovery of atmospheric chemistry and dynamics. The model output examined here consists of monthly means of many physical parameters and chemical species that characterize the state of the atmosphere. An important model output is the amount of ozone within each model cell. Ozone values were then integrated over all vertical levels to obtain ozone column density values in Dobson Units (DU).

2.3. Surface UV model

Solar UV radiation reaching the Earth surface was calculated as a function of simulated column ozone after the impact, using NCAR radiative transfer model TUV (Tropospheric Ultraviolet and Visible; Madronich and Flocke, 1997). This model computes absorption and scattering of solar radiation as it propagates through an 80 km atmospheric column, using a 4-stream discrete ordinates method (Stamnes et al., 1988), with pseudo-spherical correction for improved accuracy at low Sun conditions (Petropavlovskikh, 1995). The spectral irradiance incident at the top of the atmosphere was taken from Atlas3/SUSIM satellite measurements (Cebula et al., 1996; Woods et al., 1996; data downloaded from susim.nrl.navy.mil, 30 Sep. 1998). Standard vertical profiles for air density, temperature, and ozone, appropriate for mid-latitude annual average conditions, were taken from the US Standard Atmosphere (USSA, 1976). A Lambertian surface albedo of 5% was assumed at all wavelengths.

To assess the influence of the post-impact ozone perturbation on UV radiation at the Earth's surface, we re-scaled the standard ozone profile to the monthly mean simulated post-impact ozone column values, and evaluated wavelength-integrated spectral irradiances weighted for human erythema (skin-reddening) (McKinlay and Diffey, 1987). The calculations were performed over diurnal cycles

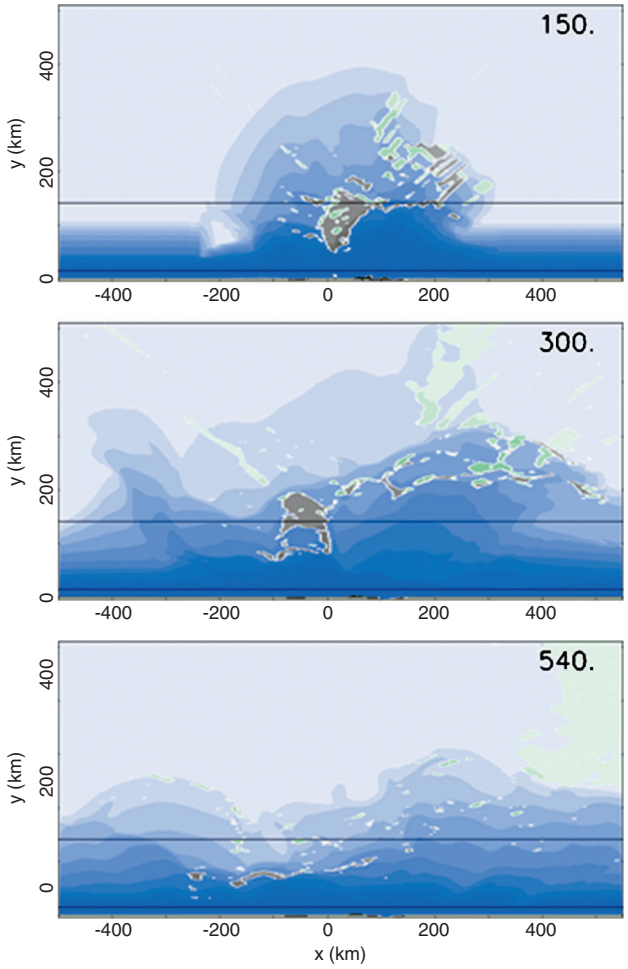

Fig. 2. Material plot in the plane of impact for the 500 m impact 2.5 min (top), 5 min (middle) and 9 min (bottom) after impact. Shade colors represent changes in density for the materials (the lighter shades corresponding to lower densities) represented by: blue — atmosphere; gray — water; green — projectile. The lowermost horizontal black line corresponds to the 15 km height, representing roughly the tropopause around the impact latitude. The uppermost horizontal black line corresponds to 140 km, which is approximately the top level of WACCM. See text for details.

for each day of the year to capture the influence of changing solar zenith angle, and were converted to monthly means following the method of Lee-Taylor et al. (2010). We neglect the effect of changing cloudiness or atmospheric aerosol content, hence any calculated UV changes are entirely due to the impact-induced ozone column changes.

3. Results and discussion

3.1. Impact simulation results

In the impact simulations water (and a small fraction of impactor) is ejected well beyond the troposphere and quickly reaches the Earth's thermosphere several hundred km above the surface. Due to the depth of the modeled ocean, crustal material (dust) is not ejected, even though the ocean floor will be scarred by the impact (mostly due to the impact-related motion of large volumes of water). Large waves will be generated at the ocean surface, possibly resulting in hazardous tsunami propagating away from the impact point. The exact damage from impact generated tsunami depends on many factors such as the proximity of the impact to coastal regions, the geometry of coastal regions, the geometry of the ocean floor, and is not addressed in this work. Recently, a detailed investigation of impact generated tsunami was presented by Weiss et al. (2006) and Wünnemann et al. (2007).

Water ejected by the impact in the atmosphere is mostly distributed in a vertical column that extends roughly over the opening cavity, and then expands outward in the upper atmosphere over a region that can reach several thousand km in diameter, slightly offset downrange of the impact point (Fig. 2). The largest component of the water is ejected in the liquid phase. A small amount of projectile material is entrained in the expansion plume as well, but it is several orders of magnitude less in mass than the water. Although we neglect this component in our simulation, impactor dust may act as condensation nuclei and accelerate the removal of liquid water from the upper atmosphere.

Simulation results indicate that about 4.4×10^{12} kg and 4.2×10^{13} kg of water (liquid plus vapor) is ejected in the middle atmosphere (>15 km) in the 500 m and 1 km asteroid impacts, respectively (see Table 1). The amount of that water shock-vaporized on impact is about 10^{12} kg for the 500 m asteroid and 10^{13} kg for the 1 km asteroid. Fig. 3 shows the amount of ejected total water, water vapor and projectile material in the upper atmosphere (>15 km) over time in terms of projectile masses (the 1 km impactor is eight times as massive as the 500 m impactor). Although the impact plume continues expanding upward and outward for several minutes after the impact (Fig. 2), the overall amount of water in the upper atmosphere changes slowly after about 2–3 min. A significant fraction of the water is ejected well into the thermosphere before falling back to the lower part of the atmosphere during plume collapse, as indicated in Fig. 2.

3.2. Atmospheric model initial conditions

Impact time and location affects the overall perturbation of atmospheric dynamics and chemistry. Upper atmospheric ozone concentration shows seasonal variability, especially at high latitudes, and the effects of an impact event may vary depending on the season when it occurs. The initial conditions for our WACCM simulations are for January 1, corresponding to Northern Hemisphere winter. High latitude impacts cause atmospheric perturbations that may be confined to the hemisphere of impact, while atmospheric perturbations from tropical impacts are more likely to be spread to both hemispheres, thus having a global effect. We chose the subtropical Northern Pacific, at a latitude of 30°N and longitude of 180°E (the dateline), as the site of our

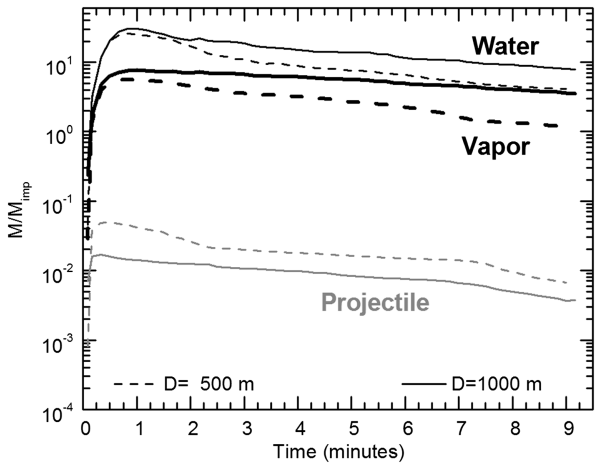

Fig. 3. Normalized mass (mass divided by incoming projectile mass) of liquid water (water — black lines), water vapor (vapor — thick black lines) and impactor (projectile — gray lines) injected into the upper atmosphere, above 15 km, during the impact of a 1 km (solid lines) and 500 m (dashed lines) asteroid. Incoming impactor masses are 1.4×10^{12} kg for the 1 km asteroid, and 1.7×10^{11} kg for the 500 m asteroid.

impacts. All WACCM simulations were carried out at horizontal resolution of 1.9°×2.5° (latitude vs. longitude).

Impact-produced water vapor, nitric oxide (NO), and halogens (Cl and Br) were added to a region around the impact site as perturbation to the steady state trace gases at the beginning of the simulation. MOZART-3 assumes that, aside from the main constituents of the atmosphere, all chemical species are present in trace amounts, consistent with a mixing ratio below about 10^{-3} (1000 parts per million by volume, ppmv). Mixing ratios much above this limit are inconsistent with the numerical formulation of the model and may produce unrealistic results. To maintain its mixing ratio below 10^{-3}, we have distributed the impact-generated water vapor over a region extending over 11×11 and 31×31 WACCM cells (~2200×2200 km and ~6200×6200 km in latitude and longitude) for the 500 m and 1 km asteroid impacts, respectively. This region is about 2 to 3 times the size of the region covered by the impact plume at the end of our impact simulations, 9 minutes after impact (Fig. 2); at that time, however, the impact plume was still expanding horizontally in the simulations.

3.2.1. Impact-ejected water

We have made the conservative assumption that liquid water quickly precipitates and will not participate in the chemistry of the atmosphere. A significant fraction of the ejected liquid water may be thermodynamically close to or above the incipient vaporization threshold, and may in fact impact atmospheric chemistry (e.g., Birks et al., 2007). On the other hand, as pointed out in Section 3.1, ejected dust from the impactor (as well as oceanic salt particles) may act as condensation nuclei, accelerating water condensation and removal in the upper atmosphere. We also neglect any impact-ejected water that remains in the troposphere (<15 km). Tropospheric water has a residence time of about 10 days (e.g., Curry and Webster, 1999); thus, we expect that any water in the troposphere will be quickly removed as rain without affecting the chemistry of the (upper) atmosphere.

The evolution of material ejected on impact, shown in Fig. 3, suggests that most of it is injected into the upper atmosphere within the first minute after the impact. After that time, the impact plume continues to expand upward (vertically) and outward (horizontally); eventually, material begins to fall while continuing to expand outward. For the atmospheric simulations we placed the amount of water vapor between about 15 km and the upper vertical limit of the WACCM domain, around 140 km. Over time, water vapor flows in and out of the atmospheric domain causing some fluctuation in the amount of water vapor in the region of interest. The overall trend is a slow decrease in the amount of water vapor, which is expected as the plume begins to settle downward. About 9 min after impact ~10% of the water vapor ejected initially is still above 140 km in the 1 km impact, and the amount of water vapor in the domain of interest (15–140 km) has decreased by about 25%. In the 500 m impact, less than 1% of the water vapor remains beyond 140 km after 9 minutes, with about 50% remaining between 15 and 140 km.

3.2.2. Impact-produced NO

NO is produced in air heated to high temperatures. This has been shown to occur during lightning discharges (Chameides, 1986) and within the fireballs of thermonuclear explosions (Foley and Rudeman, 1973; Johnston et al., 1973). The impact of asteroids or comets also produces significant amounts of NO by shock-heating air at various times during impact, from the passage of the impactor through the atmosphere, to the interaction of the atmosphere with the expanding ejecta plume, to ejecta reentering the atmosphere from above (e.g., Prinn and Fegley, 1987; Zahnle, 1990). For the projectile sizes investigated here the most important NO production phase is the interaction of the expanding impact plume with the atmosphere, as emphasized by Birks et al. (2007). Air initially shocked during projectile entry would be re-shocked soon after, as the plume expands outward, reprocessing the initially produced NO. On the other hand, significant NO production from ejecta re-entering the atmosphere from above occurs only for large impact events (such as the Cretaceous–Paleogene, K–Pg, impact event; Zahnle, 1990) which are beyond the sizes investigated here. Estimating the amount of NO produced in an impact depends on several poorly-constrained assumptions. Estimates of NO production in the K–Pg impact by Zahnle (1990) are about 6 times lower than those in Prinn and Fegley (1987), due in part to the choice of a lower quenching temperature (1700 K versus 2000 K), and in part to geometric considerations (e.g., spherical versus flat Earth).

To include the effect of impact-produced NO in the atmospheric model we follow the approach by Birks et al. (2007), who estimated that the mass of NO generated by the expanding plume is about one thousandth the mass of water vapor injected in the upper atmosphere:

$$m_{NO} \sim 10^{-3} \times m_{H2O} \quad (1)$$

This estimate, based on calculations by Prinn and Fegley (1987) may represent an upper bound for the NO produced in the impact.

3.2.3. Impact-produced halogens

Seawater contains dissolved salts, with an average concentration around 34.5‰ (parts per thousand by weight; Curry and Webster, 1999). The most abundant ions are chloride (Cl^-), which occurs at concentrations of about 19‰, and sodium (Na^+), at concentrations near 10.5‰. Among the halogens, besides chloride, bromide (Br^-) is a minor component of dissolved salts (0.065‰) while fluoride (F^-), and iodide (I^-) are presents in trace amounts (<1 ppmv).

The injection of large amounts of chemically activated halogens from sea salt contained in vaporized sea water can produce significant stratospheric ozone depletion. Vaporized salts would initially condense into sub-micron particles containing chlorine and bromine. In the upper atmosphere condensation of ice onto the particles would prevent the growth of the salt nuclei. Subsequent evaporation of the ice would then free the salt particles during transport downward toward denser regions of the atmosphere where chloride and bromide can be oxidized into gaseous chlorine- and bromine-containing species (e.g., Birks et al., 2007).

The chemistry package included in WACCM does not include the oxidation reactions needed to oxidize halogen salts. However, based on the discussion in Birks et al. (2007) and on the abundance of HNO_3 in the stratosphere, we estimate that the most common oxidation reaction for Cl and Br in the upper atmosphere results in the formation of hydrogen chloride (HCl) and hydrogen bromide (HBr). These gases do not interact directly with ozone but can be converted to more reactive forms that chemically destroy ozone. Chlorine and bromine were thus initially introduced in WACCM as HCl and HBr. From this point on, any tranformation into other forms of Cl and Br, including the "active" species that can catalyze ozone, is handled by the chemistry package in WACCM (Kinnison et al., 2007). Following the approach of Birks et al. (2007) we estimated the masses of impact-released HCl and HBr as fractions of the oceanic water vapor mass injected into the upper atmosphere:

$$m_{HCl} \sim 2 \cdot 10^{-3} \times m_{H2O} \quad (2)$$

$$m_{HBr} \sim 3 \cdot 10^{-6} \times m_{H2O} \quad (3)$$

3.3. Atmospheric model results

WACCM simulations were carried out for 3 and 5 years after impact for the 500 m and 1 km diameter impactors. Below we document the evolution of the atmospheric column density (>15 km), as fractional changes relative to the unperturbed case, for water vapor,

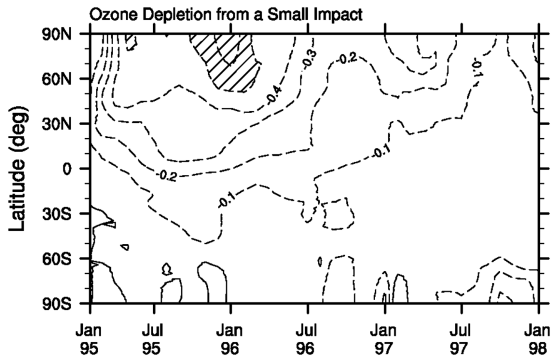

Fig. 4. Zonally averaged monthly mean fractional changes of atmospheric ozone column over 3 years following the impact of the 500 m asteroid in the Central Pacific. The values are calculated with respect to the unperturbed case, that is, (perturbed − unperturbed)/unperturbed.

total inorganic nitrogen (NO_Y) total inorganic bromine (Br_Y) and total inorganic chlorine (Cl_Y).[1] Overall, the impact perturbation of NO_Y is relatively short-lived compared to that of water vapor and especially halogens; compared with the duration of atmospheric ozone perturbations, this suggests that NO_Y has a minor effect on ozone chemistry compared to halogens.

3.3.1. 500 m asteroid impact

The impact of a 500 m asteroid increases the upper atmospheric water vapor content by more than 1.5 times the background over a wide region surrounding the impact point for the first month after the impact. Halogens, Cl_Y and Br_Y, follow the water vapor distribution, with an initial increase of over 20 and 5 times normal background, respectively, in the same region surrounding the impact. The perturbations eventually spread over the northern hemisphere, where water vapor content remains about 50% above background for the first year after impact, while Cl_Y and Br_Y exceed five times and twice their background values. The NO_Y perturbation is comparable to Br_Y at first, but it decays quickly due to conversion of nitrogen species to HNO_3 by heterogeneous processes in the polar lower stratosphere, and subsequent removal via precipitation of nitric acid trihydrate (NAT) particles (see, e.g., Kinnison et al., 2007). Overall, perturbations of the various chemical species in the upper atmosphere extend as far south as the Tropics, without significantly affecting the southern hemisphere (not shown).

The 500 m impact causes modest ozone depletion for about 1.5 years in the Northern Hemisphere (where the impact occurs), as shown in Fig. 4. The largest perturbation occurs at mid-to-high latitudes were ozone depletion of >50% occurs for a few months, with minima exceeding the recorded historic minima (~100 DU) of the springtime (South Pole) ozone hole in the mid-1990 s (Hofmann et al., 1997). Ozone concentration returns to normal after about 2.5 years in the northern hemisphere. No significant ozone depletion is recorded in the southern hemisphere.

3.3.2. 1 km asteroid impact

The impact of a 1 km asteroid increases the upper atmospheric water vapor content by more than 5 times in the northern hemisphere for the first month after the impact, while Cl_Y and Br_Y column densities increase over 100 and 30 times compared to the normal background in the region surrounding the impact, as shown in Fig. 5. As the perturbations start spreading, the northern hemisphere water vapor content remains about twice the background for the first year after impact, with Cl_Y and Br_Y exceeding background by 20 times and 10 times, respectively. The perturbation also extends to the southern hemisphere with a relatively small (<50%) increase in water vapor. Halogens become globally distributed within about a year after the impact; overall levels of Cl_Y are above 5 times background for over 3 years. Br_Y levels remain above twice the background globally for about 2.5 years. The injection of NO_Y is significant, over 3 times the background in the northern hemisphere, for the first few months after the impact but, as in the case of the 500 m impact, large NO_Y perturbations do not last more than a few months.

The strong perturbation in upper atmospheric water vapor and halogens is reflected in the evolution of atmospheric ozone. The 1 km impact results in a significant global ozone depletion that extends over the duration of the atmospheric simulation, as shown in Fig. 6. Ozone depletion reaches values >70% for more than 2 years at mid-to-high latitudes. The perturbation begins in the northern hemisphere and spreads to the southern hemisphere within a few months after the impact. Worldwide depletions of >50% occur for over one year, with minima as extreme as 20 DU at high latitudes. Mid-to-high latitudes of both hemispheres are exposed to continuous ozone depletion >40% for about 3.5 years. Recovery is slow and begins in the Tropics, where only a mild ozone depletion of 10–20% remains about 3 years after the impact. Ozone levels begin to recover sooner at northern high-latitudes than at southern high-latitudes.

The absorption of UV radiation by ozone is the main source of heat in the stratosphere and mesosphere (Brasseur and Solomon, 2005). It is not surprising, therefore, that ozone depletion in the upper atmosphere is accompanied by significant cooling. The 1 km asteroid impact causes strong cooling for about 3 years in the stratosphere and mesosphere, with annual zonal mean temperatures decreasing by more than 20 K in the lower stratosphere. The smaller ozone depletion in the 500 m asteroid impact results in a milder stratospheric cooling, with values ~10 K in the tropical regions and mid-northern latitudes for the first year after the impact. However, the cooling is limited to the upper atmosphere, and does not extend to the troposphere. Thus, in both impact events surface temperatures are not affected by the significant perturbations of the upper atmosphere. However, it is important to note that these calculations do not address the impact of ejected particulates, which would be expected to intercept solar radiation and lead to tropospheric temperature changes. While injection of particulates is negligible for a oceanic impact if the ocean floor is not cratered, as in the case of the impacts modeled here, that would not be the case for impacts on land.

3.4. UV model results

Ozone is a strong absorber of UV radiation, especially UV-B (280–315 nm; UNEP, 2003). In the Earth's atmosphere, 90% of ozone is concentrated in the stratosphere between about 10 and 50 km from the surface. This ozone provides a natural sunblock to UV experienced at the Earth's surface. Indeed, there is a well-established inverse correlation between ozone and UV-B irradiance at the Earth's surface (UNEP, 2003). The removal of a significant amount of ozone in the upper atmosphere for an extended period of time can have important biologic repercussions at the Earth's surface as a consequence of increase in surface UV-B irradiance. These include increased incidence of erythema (skin-reddening), cortical cataracts, changes in plant growth, and changes in molecular DNA (e.g., UNEP, 2003).

Since the most common result of UV-B over-exposure for humans is sunburn, the intensity of UV irradiance at the Earth's surface is usually reported to the general public using the international UV Index (UVI) (WHO, 2002). This measure is based on the local solar noontime value of the erythemally-weighted UV irradiance, which takes into account the wavelength dependence of the effectiveness of

[1] The NO_Y, Cl_Y and Br_Y chemical families are defined as follows: $NO_Y = N + NO + NO_2 + NO_3 + 2N_2O_5 + HO_2NO_2 + HNO_3 + BrONO_2 + ClONO_2$; $Cl_Y = Cl + 2Cl_2 + ClO + OClO + 2Cl_2O_2 + HOCl + ClONO_2 + HCl + BrCl$; and $Br_Y = Br + BrO + BrCl + HOBr + BrONO_2 + HBr$.

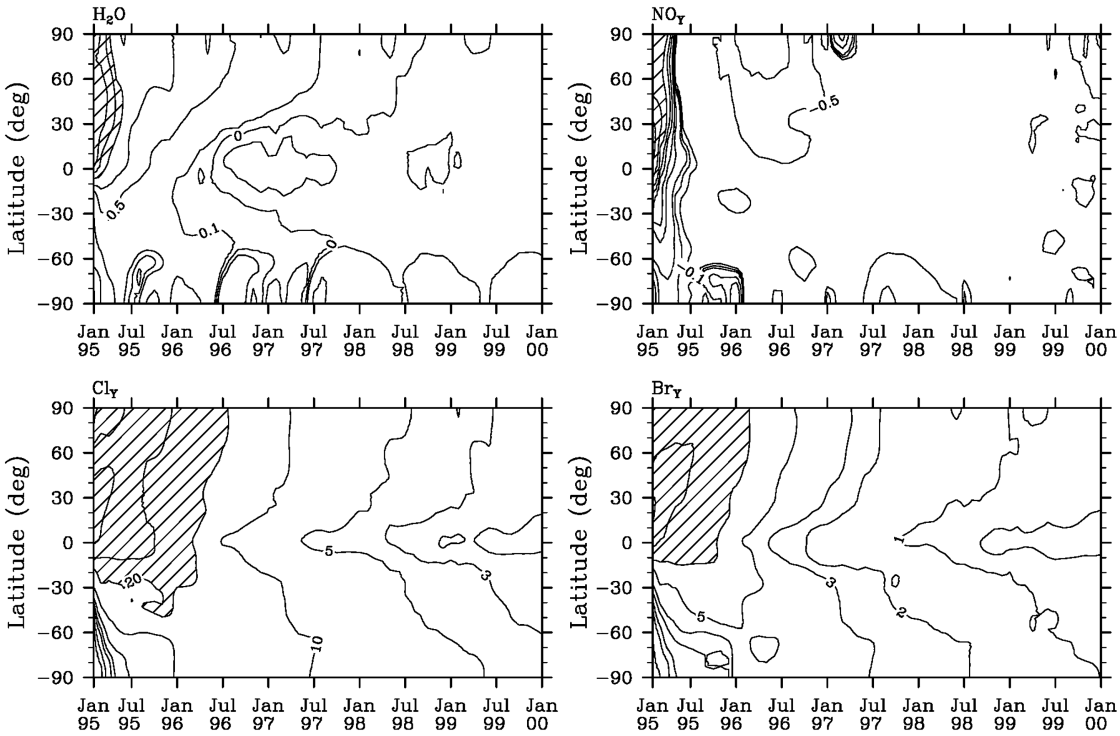

Fig. 5. Time evolution of the zonally averaged column density of water vapor, NO_Y, Cl_Y, and Br_Y, relative to the 1 km asteroid impact into a 4 km deep ocean. The values are calculated with respect to the unperturbed case, that is, (perturbed − unperturbed)/unperturbed.

UV irradiance in causing sunburn, and is scaled by a constant factor to produce values on a nominal scale. UVI values >10 are characterized as 'extreme', and accompanied by a warning that unprotected skin (especially for light-skinned people) can burn in minutes. Such values are typically found equator wards of ~45° at the peak of summer, and are confined to the tropics in winter. Typical year-round equatorial values are in the range 13 to 16, with maxima around 18. Exceptionally high values up to 20 have been recorded on certain days in the intertropical high altitude desert of Puna de Atacama, in Argentina, due to a combination of small solar zenith angle and a very clean and dry atmosphere.

Projected changes in surface-level UV irradiance track projected ozone column changes both in timing and location. The strongest relative changes occur for the 1 km asteroid impact at northern mid-to-high latitudes during the first two years after the impact, with erythemally-weighted UV levels over 5 times above normal; increases of a factor of two or more are seen throughout the northern hemisphere for much of the first two years (Fig. 7). Similar increases occur in southern extra-tropical latitudes for a few years, so that the UV-B environment is significantly altered worldwide for a substantial period. At the same time, UV-A irradiance is not affected by ozone depletion.

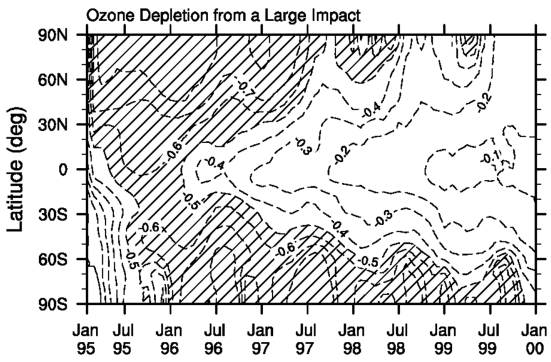

Fig. 6. As in Fig. 4, but for the 1 km impact case.

In the 500 m asteroid impact the change to surface level UV-B irradiance is significantly smaller (not shown). Erythemally weighted UV levels up to 3 times above normal are limited to northern high latitudes (>50°) for less than one year, and levels 50% above normal persist at mid-to-high latitudes for about 1.5 years. Following the trend of ozone, there is little change in surface UV irradiance in the southern hemisphere.

Fig. 8 presents the time evolution of UV irradiance expressed in terms of UVI for the impact-perturbed and unperturbed simulations. While the strongest relative changes in UV are seen at high latitudes (e.g., Fig. 7), the strongest absolute changes occur at lower latitudes where unperturbed UV is strongest. In the small impact simulation, the distribution of UVI values >10 is quite similar to the control case; however, the magnitude of the tropical peak values is considerably larger, remaining above 20 for several months in the northern subtropics, and reaching a maximum of 25 at 27°N, 7 months after the impact. In the large impact case, values exceeding 20, that is, greater than currently experienced anywhere on earth, are widespread for the first 2 years following the impact, reaching 70° latitude in each summer hemisphere, with a peak value of 56 around 27°N.

3.5. Effects of increased UV-B irradiance

The consequence of a large and prolonged increase in UV-B radiation on living organisms is difficult to address, as it has never been recorded in the past. Investigations of the effects of increased UV-B exposure on living organisms began soon after the first

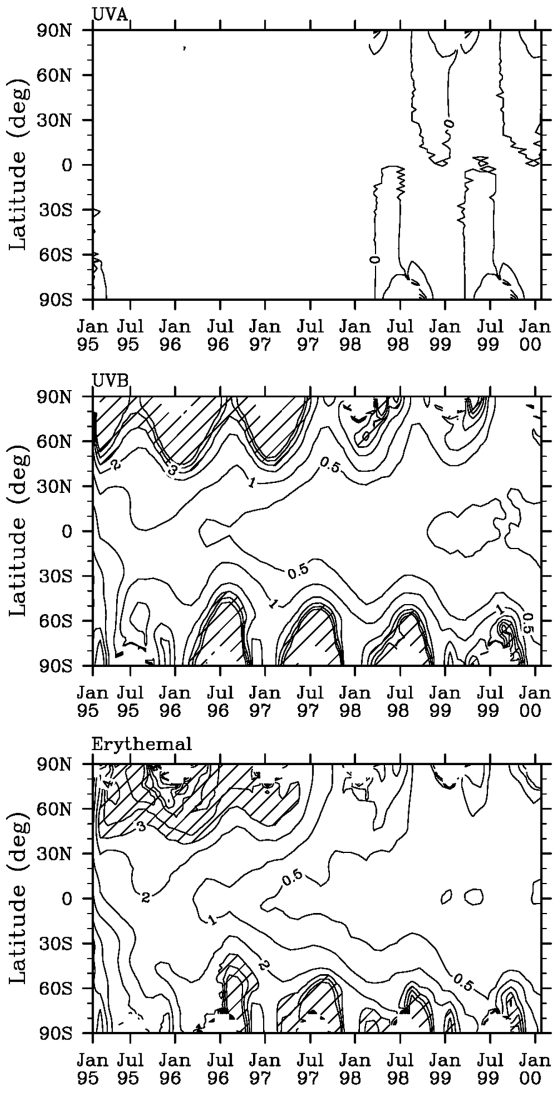

Fig. 7. Increase in surface UV radiation, broken down into UV-A (315–400 nm), UV-B (290–315 nm) and Erythemal UV for the 1 km asteroid impacting the Central Pacific. Values are normalized to the unperturbed case: (perturbed − unperturbed)/unperturbed.

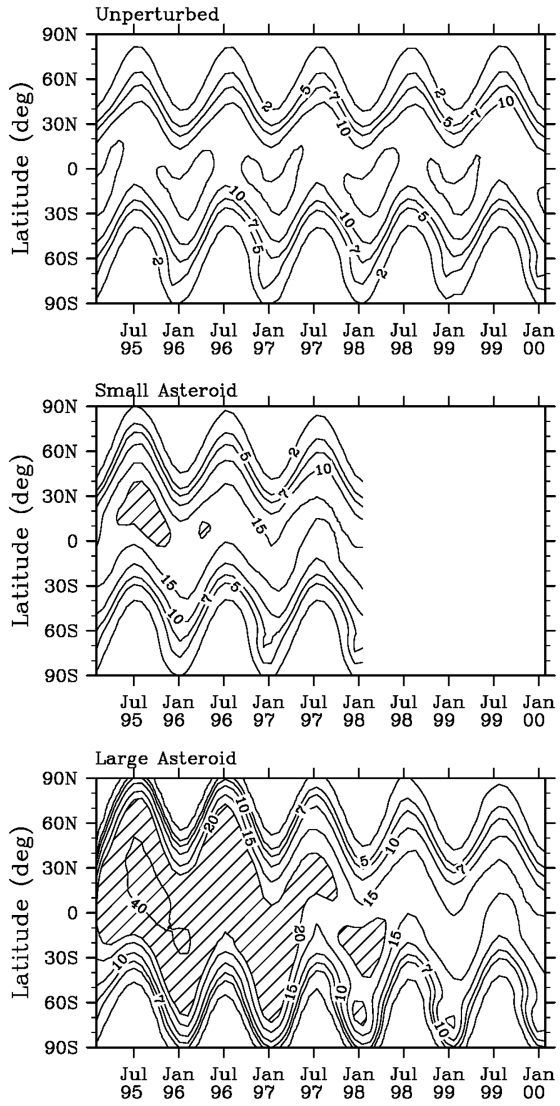

Fig. 8. Time evolution of the zonally averaged UV Index (dimensionless) over time for the unperturbed atmosphere (top), a perturbed atmosphere after a 500 m asteroid impact (middle) and a perturbed atmosphere after a 1 km asteroid impact (bottom).

suggestion of stratospheric ozone reduction (e.g., Crutzen, 1972). Terrestrial animal life may be partially protected from the damaging effects of solar UV, either by their behavioral patterns or by UV-opaque body coverings (such as furs, feathers, etc.). For humans, sunscreens are very effective in protecting against sunburn; they also help reduce the incidence of skin cancer.

Plants constitute most of the living mass in terrestrial ecosystems (Caldwell et al., 1995). The dependence on sunlight for survival and the inability to move make higher plants particularly susceptible to increased UV-B irradiance. While responses may vary considerably for different plant species, recorded general effects of increased UV-B exposure include plant height reduction, decreased shoot mass, and reduction in foliage area (Caldwell et al., 2003). Overall, most plants have a remarkable capacity to respond to increased UV-B levels by both increasing UV-protection via the production of UV-screening pigments (typically flavonoids) and repairing damage to DNA molecules (e.g., due to production of pyrimidine dimers) via the photoactivated enzyme DNA photolyase (e.g., Caldwell et al., 1995). During extended increased UV-B exposure, however, not all DNA damage may be fully repaired; as a result, damage may accumulate over time and carry-over to following plant generations, affecting the genetic stability of plants by increasing the frequency of mutations (e.g., Walbot, 1999).

In addition to the direct effects of increased UV-B exposure, indirect effects can also be important, even if less predictable. They include changes in the susceptibility of plants to attack by insects and pathogens and changes in competitive balance of plants and nutrient cycling (e.g., Mpoloka, 2008). Enhanced UV-B radiation may also affect important soil surface processes, such as nitrogen fixation by cyanobacteria (Solheim et al., 2002). All these effects may decrease the productivity of agricultural regions worldwide and have important consequences on human sustainability. There are large differences in UV-B response among cultivars studied so far (most exhibit sensitivity to UV-B, although some are UV tolerant; Caldwell et al., 1995), but UV-B sensitivity has not yet been considered a selective factor for plant breeders (Mpoloka, 2008).

Over 30% of the world's animal protein for human consumption comes from the sea, mostly in the form of finfish, shellfish and seaweed, and particularly in the developing countries, this percentage can be significantly higher (Hader et al., 1995). Increased UV-B levels associated with Antarctic ozone hole levels have been shown to inhibit phytophankton activity in the upper ocean layer (Smith et al., 1992). Phytoplankton is the foundation on which the very survival of aquatic food webs depends. They are mostly concentrated at high latitudes whereas, except for upwelling areas on the continental shelves, the tropics and subtropics have up to 100 times lower concentrations (Hader et al., 1995). Hader et al. (1995) estimated that a 16% ozone depletion could result in a 5% loss in phytoplankton, which, based on estimates of Nixon (1988), could cause a reduction in fishery and aquaculture yields of about 7% and a loss of about 7 million tons of fish per year. Solar UV-B radiation has also been found to cause damage to early developmental stages of fish, shrimp, crab and other animals. The most severe effects are decreased reproductive capacity and impaired larval development (USEPA, 1987).

Looking back at the Earth's past, an exciting new botanical proxy to investigate past changes in atmospheric ozone concentration, recently suggested by Lomax et al. (2008), may help identify potential ecological changes associated with prolonged impact related ozone depletion. Lomax et al. (2008) showed that concentration of two UV-B absorbing components of the complex biomacromolecule that forms the outer walls of pollen and spores of two species of clubmosses (Lycophyta) increases with increased UV-B exposure. They were able to correlate variations in these UV-B absorbing compounds at mid to high latitude locations with recent decadal declines in growing-season total ozone and reconstructed documented changes in growing season ozone column over the past century from well-dated spore archives. Medium size oceanic impacts may cause important ecological changes over several years as a result of enhanced UV-B fluxes at the surface. As described in Birks et al. (2007), this may occur at intervals of ~160–200 kyr and ~700–800 kyr for oceanic impacts of 500 m and 1 km diameter objects respectively. Although ozone changes can also be associated with a variety of natural phenomena, including changes in solar radiation, volcanic eruptions and climate-change related processes, each of these processes has its own characteristic temporal and spatial scales. Therefore, the availability of single taxa spore/pollen sequences combined with accurate inspection of the geologic record may ultimately help identify evidence for past environmental perturbations associated with mid size asteroid impacts.

4. Conclusion

We have calculated the perturbation to atmospheric chemistry occurring after the impact of medium size asteroids, 500 m and 1 km in diameter, in the northern subtropical Pacific ocean. We characterize atmospheric chemistry perturbations by following the evolution of upper atmospheric ozone. Overall, our results indicate that:

- Mid-latitude oceanic impact of asteroids 1 km in diameter can produce a significant, global perturbation of upper atmospheric chemistry; asteroids 500 m in diameter cause only minor perturbation of upper atmospheric chemistry, limited to the hemisphere in which the impact occurred;
- Several years of ozone depletion comparable to Antarctic ozone hole records observed in the mid-1980 s and 1990 s, occur worldwide as a consequence of mid-latitude oceanic impact of asteroids 1 km in diameter;
- Impact-induced ozone depletion affects UV irradiance at the Earth's surface, resulting in UV-B levels that can be dangerous for living organisms. In the Tropics, and in midlatitude summers immediately after the impact, UV-B greatly exceeds the highest levels currently experienced anywhere on Earth;
- While it is difficult to establish a quantitative relation between increased surface UV-B levels and its effect on living organisms, current understanding of the sensitivity of ecosystems to increased UV-B levels suggests that the oceanic impact of a 1 km asteroid would have a long-lasting negative impact on global food production, which, in turn, may affect the sustainability of the current human population.

The present calculations do not address the impact of ejected particulates, which are expected to play a minor role in oceanic impacts such as those considered here. However, the effects of suspended particles on surface climate would be the most dramatic consequence of land impacts.

Acknowledgments

We thank two anonymous reviewers, whose comments and suggestions helped us improve the final manuscript. This work is supported by NASA grant NNX09AM83G.

References

Alvarez, L.W., Alvarez, W., Asaro, F., Michel, H.V., 1980. Extraterrestrial cause for the Cretaceous–Tertiary extinction. Science 208, 1085–1108.
Birks, J.W., Crutzen, P.J., Roble, R.G., 2007. Frequent Ozone Depletion Resulting from Impacts of Asteroids and Comets. In: Bobrowsky, P., Rickman, H. (Eds.), Comet/Asteroid Impacts and Human Society. Springer Pub, Berlin, pp. 225–245.
Bottke Jr., W.F., Morbidelli, A., Jedicke, R., Petit, J.-M., Levison, H.F., Michel, P., Metcalfe, T., 2002. Debiased orbital and absolute magnitude distribution of the Near-Earth Obiects. Icarus 156, 399–433.
Brasseur, G.P., Solomon, S., 2005. Aeronomy of the middle atmosphere. Springer Pub, Dordrecht, The Netherlands. 644 pp.
Caldwell, M.M., Teramura, A.H., Tevini, M., Bornman, J.F., Björn, L.O., Kulandaivelu, G., 1995. Effects of increased solar ultravioled radiation on terrestrial plants. Ambio 24 (3), 166–173.
Caldwell, M.M., Ballaré, C.I., Bornman, J.F., Flint, S.D., Björn, L.O., Teramura, A.H., Kulandaivelu, G., Tevini, M., 2003. Terrestrial ecosystems, increased solar ultraviolet radiation and interaction with other climatic change factors. UNEP special issue. Photochem. Photobiol. Sci. 2, 29–38.
Cebula, R.P., Thuiller, G.O., VanHoosier, M.E., Hilsenrath, E., Herse, M., Brueckner, G.E., Simon, P.C., 1996. Observations of the solar irradiance in the 200–350 nm interval during the ATLAS-1 Mission: A comparison among three sets of measurements-SSBUV, SOLSPEC, and SUSIM. GRL 23 (17), 2289–2292.
Chameides, W.L., 1986. The Role of Lightning in the Chemistry of the Atmosphere. In The Earth's electrical environment. Nat. Acad. Press, Washington, pp. 70–77.
Chapman, C.R., Morrison, D., 1994. Impact on the Earth by asteroids and comets: assessing the hazard. Nature 367, 33–40.
Chyba, C.F., 1991. Terrestrial mantle siderophiles and the lunar impact record. Icarus 92, 217–233.
Collins, W.D., Rash, P.J., Boville, B.A., Hack, J.J., McCaa, J.R., Williamson, D.L., Kiehl, J.T., Briegleb, B., Bitz, C., Lin, S.-J., Zhang, M., Dai, Y., 2004. Description of the NCAR Community Atmospheric Model (CAM 3.0). Technical Report NCAR/TN-464+STR (National Center for Atmospheric Research, Boulder, CO).
Crutzen, P.J., 1972. SSTs — a threat to the Earth's ozone shield. Ambio 4, 41–51.
Curry, J.A., Webster, P.J., 1999. Thermodynamics of atmospheres and oceans. Int. Geophys, vol. 65. Academic Press, New York, p. 471. Series.
Eyring, V., Cionni, I., Bodeker, G.E., Charlton-Perez, A.J., Kinnison, D.E., Scinocca, J.F., Waugh, D.W., Akiyoshi, H., Bekki, S., Chipperfield, M.P., Dameris, M., Dhomse, S., Frith, S.M., Garny, H., Gettelman, A., Kubin, A., Langematz, U., Mancini, E., Marcharnd, M., Nakamura, T., Oman, L.D., Pawson, S., Pitari, G., Plummer, D.A., Rozanov, E., Shepherd, T.G., Shibata, K., Tian, W., Braesicke, P., Hardiman, S.C., Lamarque, J.F., Morgenstern, O., Pyle, J.A., Smale, D., Yamashita, Y., 2010. Multi-model assessment of ozone recovery and sensitivity of ozone return dates to greenhouse gas scenarios, ACPD 10, 11659–11710. www.atmos-chem-phys-discuss.net/10/11659/2010/acpd-10-11659-2010.pdf.
Eyring, V., Butchart, N., Waugh, D.W., Akiyoshi, H., Austin, J., Bekki, S., Bodeker, G.E., Boville, B.A., Brühl, C., Chipperfield, M.P., Cordero, E., Dameris, M., Deushi, M., Fioletov, V.E., Frith, S.M., Garcia, R.R., Gettelman, A., Giorgetta, M.A., Grewe, V., Jourdain, L., Kinnison, D.E., Mancini, E., Manzini, E., Marchand, M., Marsh, D.R., Nagashima, T., Newman, P.A., Nielsen, J.E., Pawson, S., Pitari, G., Plummer, D.A., Rozanov, E., Schraner, M., Shepherd, T.G., Shibata, K., Stolarski, R.S., Struthers, H., Tian, W., Yoshiki, M., 2006. Assessment of temperature, trace species, and ozone in chemistryclimate model simulations of the recent past. J. Geophys. Res. 111 (D22 308). doi:10.1029/2006JD007327.
Eyring, V., Waugh, D.W., Bodeker, G.E., Cordero, E., Akiyoshi, H., Austin, J., Beagley, S.R., Boville, B., Braesicke, P., Brühl, C., Butchart, N., Chipperfield, M.P., Dameris, M., Deckert, R., Deushi, M., Frith, S.M., Garcia, R.R., Gettelrman, A., Giorgetta, M., Kinnison, D.E., Mancini, E., Manzini, E., Marsh, D.R., Matthes, S., Nagashima, T., Newman, P.A., Pawson, S., Pitari, G., Plummer, D.A., Rozanov, E., Schraner, M., Scinocca, J.F., Semeniuk, K., Shepherd, T.G., Shibata, K., Steil, B., Stolarski, R., Tian,

W., Yoshiki, M., 2007. Multi-model projections of stratospheric ozone in the 21st century. J. Geophys. Res. 112 (D16303). doi:10.1029/2006JD008332.
Foley, H.M., Rudeman, M.A., 1973. Stratospheric NO production from past nuclear explosions. JGR 78, 4441–4451.
Garcia, R.R., Marsh, D.R., Kinnison, D.E., Boville, B.A., Sassi, F., 2007. Simulation of secular trends in the middle atmosphere, 1950–2003. JGR 112, D09301. doi:10.1029/2006JD007485.
Hader, D.P., Worrest, R.C., Kumar, H.D., Smith, R.C., 1995. Effects of increased solar ultravioled radiation on acquatic ecosystems. Ambio 24, 174–180.
Harris, A., 2008. What Spaceguard did. Nature 453, 1178–1179.
Hofmann, D.J., Oltmans, S.J., Harris, J.M., Johnson, B.J., Lathrop, J.A., 1997. Ten years of ozone-sonde measurements at the south pole: implications for recovery of springtime Antarctic ozone. J. Geophys. Res. 102, 8931–8943.
Johnston, H.S., Whitten, G., Birks, J., 1973. Effect of nuclear explosions on stratospheric nitric oxide and ozone. JGR 78, 175–186.
Kinnison, D.E., Brasseur, G.P., Walters, S., Garcia, R.R., Marsh, D.R., Sassi, F., Harvey, V.L., Randall, C.E., Emmons, L., Lamarque, J.F., Hess, P., Orlando, J.J., Tie, X.X., Randel, W., Pan, L.L., Gettelman, A., Granier, C., Diehl, T., Niemeier, U., Simmons, A.J., 2007. Sensitivity of chemical tracers to meteorological parameters in the MOZART-3 chemical transport model. JGR 112 (D20302). doi:10.1029/2006JD007879.
Lee-Taylor J., Madronich S., Mayer B., Fischer C., 2010. A Climatology of UV Radiation, 1979–2000, 65 S - 65 N, Chapter 1 in UV Radiation in Global Climate Change: Measurements, Modeling and Effects on Ecosystems (Gao, W., D. Schmoldt, J.R. Slusser Eds.), Springer-Verlag (Heidelberg), and Tsinghua University Press (Beijing), 1–20.
Lin, S.-J., 2004. A vertically Lagrangian finite-volume dynamical core for global models. Mon. Weath. Rev. 132, 2293–2307.
Lomax, B.H., Fraser, W.T., Sephton, M.A., Callaghan, T.V., Self, S., Harfoot, M., Pyle, J.A., Wellman, C.H., Beerling, D.J., 2008. Plant spore walls as a record of long-term changes in ultraviolet-B radiation. Nat. Geosci. 1, 592–596.
Madronich, S., Flocke, S., 1997. Theoretical Estimation of Biologically Effective UV Radiation at the Earth's Surface. In: Zerefos, C. (Ed.), Solar Ultraviolet Radiation—Modeling, Measurements and Effects. : NATO ASI, vol. 152. Springer-Verlag, Berlin, pp. 23–48. Series.
McKinlay, A.F., Diffey, B.L., 1987. A Reference Action Spectrum for Ultraviolet Induced Erythema in Human Skin. In: Passchier, W.R., Bosnjakovic, B.F.M. (Eds.), Human Exposure to Ultraviolet Radiation: Risks and Regulations. Elsevier, Amsterdam, pp. 83–87.
Morrison, D., Harris, A.W., Sommer, G., Chapman, C.R., Carusi, A., 2002. Dealing with the Impact Hazard. In: Bottke, W.F., Cellino, A., Paolicchi, P., Binzel, R.P. (Eds.), Asteroids III. Univ. of Arizona Press, Tucson, pp. 739–754.
Mpoloka, S.W., 2008. Effects of prolongued UV-B exposure in plants. African J. Biotech. 7 (25), 4874–4883.
Nixon, S.W., 1988. Physical energy inputs and the comparative ecology of lake and marine ecosystems. Limnol. Oceanogr. 33, 1005–1025.
Petropavlovskikh I., 1995. Evaluation of photodissociation coefficient calculations for use in atmospheric chemical models. Ph. D. Thesis, U. of Brussels and NCAR/CT-159, Boulder, 1995.
Pierazzo, E., Melosh, H.J., 2000. Understanding oblique impacts from experiments, observations, and modeling. Ann. Rev. Earth Planet. Sci. 28, 141–167.
Pierazzo, E., Vickery, A.M., Melosh, H.J., 1997. A reevaluation of impact melt production. Icarus 127, 408–423.
Pierazzo, E., Kring, D.A., Melosh, H.J., 1998. Hydrocode simulation of the Chicxulub impact event and the production of climatically active gases. JGR, 103, pp. 28607–28625.
Pierazzo, E., Artemieva, N., Asphaug, E., Baldwin, E., Cazamias, J., Coker, R., Collins, G.S., Crawford, D.A., Davison, T., Elbeshausen, D., Holsapple, K.A., Housen, K.R., Korycansky, D.G., Wünnemann, K., 2008. Validation of numerical codes for impact and explosion cratering. Meteoritics Planet. Sci. 43 (12), 1917–1938.
Pilcher, C., 1998. Testimony before House Subcommittee on Space and Aeronautics. http://www.house.gov/science/pilcher_05?21.htm1998.
Prinn, R.J., Fegley, J.B., 1987. Bolide impacts, acid rain, and biospheric traumas at the Cretaceous–Tertiary boundary. Earth Planet. Sci. Lett. 83, 1–15.
Roble, R.G., Ridley, E.C., 1994. A thermosphere, ionosphere, mesosphere, electrodynamics general circulation model (TIME/GCM): equinox solar cycle simulations (30–500 km). Geophys. Res. Lett. 21, 417–420.
Schulte, P., Alegret, L., Arenillas, I., Arz, J.A., Barton, P., Bown, P.R., Bralower, T.R., Christeson, G.L., Claeys, P., Cockell, C.S., Collins, G.S., Deutsch, A., Goldin, T.J., Goto, K., Grajales-Nishimura, J.M., Grieve, R.A.F., Gulick, S., Johnson, K.R., Kiessling, W., Koeberl, C., Kring, D.A., MacLeod, K.G., Matsui, T., Melosh, H.J., Montanari, A., Morgan, J.V., Neal, C.R., Nichols, D.J., Norris, R.D., Pierazzo, E., Ravizza, G., Rebolledo-Vieyra, M., Reimold, W.U., Robin, E., Salge, T., Speijer, R.P., Sweet, A.R., Urrutia-Fucugauchi, J., Vajda, V., Whalen, M.T., Willumsen, P.S., 2010. The Chicxulub asteroid impact and mass extinction at the Cretaceous–Paleogene boundary. Science 327, 1214–1218. doi:10.1126/science.1177265.
Seinfeld, J.H., Pandis, S.N., 1998. Atmospheric Chemistry and Physics — From Air Pollution to Climate Change. Wiley and Sons, New York. 1326 pp.
Shuvalov, V.V., 1999. Multi-dimensional hydrodynamic code SOVA for interfacial flows: application to thermal layer effect. Shock Waves 9, 381–390.
Smith, R.C., Prezelin, B.B., Baker, K.S., Bidigare, R.R., Boucher, N.P., Coley, T., Karentz, D., MacIntyre, S., Matlick, H.A., Menzies, D., Ondrusek, M., Wan, Z., Waters, K.J., 1992. Ozone depletion: ultraviolet radiation and phytoplankton biology in Antarctic waters. Science 255, 952–959.
Solheim, B., Johanson, U., Callaghan, T.V., Lee, J.A., Gwynn-Jones, D., Björn, L.O., 2002. The nitrogen fixation potential of arctic cryptogram species is influenced by enhanced UV-B radiation. Oecologia 133, 90–93.
SPARC CCMVal, 2010. SPARC CCMVal Report on the Evaluation of Chemistry-Climate Models, V. Eyring, T. G. Shepherd, D. W. Waugh (Eds.), SPARC Report No. 5, WCRP-X, WMO/TD-No. X, http://www.atmosp.physics.utoronto.ca/SPARC.
Stamnes, K., Tsay, S., Wiscombe, W., Jayaweera, K., 1988. A numerically stable algorithm for discrete-ordinate-method radiative transfer in multiple scattering and emitting layered media. Appl. Opt. 27, 2502–2509.
Stokes, G.H., Yeomans, D.K., Bottke Jr., W.F., Chesley, S.R., Gold, R.E., Harris, A.W., Jewitt, D., Kelso, T.S., McMillan, R.S., Spahr, T.B., Worden, S.P., 2003. Study to determine the feasibility of extending the search for near-Earth objects to smaller limiting diameters. NASA Report. 154 pp. http://neo.jpl.nasa.gov/neo/neoreport030825.pdf.
Thompson S. L. and Lauson H.S., 1972. Improvements in the Chart D radiation-hydrodynamic CODE III: Revised analytic equations of state. Report SC-RR-71 0714. Albuquerque: Sandia National Laboratory, 119 p.
Turtle, E.P., Pierazzo, E., 2001. Thickness of a Europan ice shell from impact crater simulations. Science 294, 1326–1328.
UNEP, 2003. UNEP environmental effects of ozone depletion and its interactions with climate change: 2002 assessment. Special Issue, Photochem. Photobiol. Sci 2.
USEPA, 1987. (US Environmental Protection Agency). An assessment of the effects of ultraviolet-B radiation on aquatic organisms. Assessing the Risks of Trace Gases That Can Modify the Stratosphere. EPA 400/1-87/OOlC, pp. 1–33.
USSA (US Standard Atmosphere), 1976. National Oceanic and Atmospheric Administration (NOAA), National Aeronautics and Space Administration (NASA), United States Air Force, Washington DC.
Walbot, V., 1999. UV-B damage amplified by transposons in maize. Nature 397, 398–399.
Weiss, R., Wünnemann, K., Bahlburg, H., 2006. Numerical modelling of generation, propagation and run-up of tsunamis caused by oceanic impacts: model strategy and technical solutions. Geophys. J. Int. 167, 77–88.
WHO, 2002. Global solar UV index. A practical guide. World Health Organization, WHO/SDE/OEH/02.2. 28 pp.
Wünnemann, K., Weiss, R., Hofmann, K., 2007. Characteristics of oceanic impact-induced large water waves — re-evaluation of the tsunami hazard. Meteor. Plan. Sci. 42 (11), 1893–1903.
Woods, T.N., Prinz, D.K., Rottman, G.J., London, J., Crane, P.C., Cebula, R.P., Hilsenrath, E., Brueckner, G.E., Andrews, M.D., White, O.R., VanHoosier, E., Floyd, L.E., Herring, L.C., Knapp, B.G., Pankratz, C.K., Reiser, P.A., 1996. Validation of the UARS solar ultravioled irradiances: Comparison with the ATLAS 1 and 2 measurements. JGR 101 (D6), 9451–9569.
Zahnle, K.J., 1990. Atmospheric Chemistry by Large Impacts. In Global Catastrophes in Earth's history; An Interdisciplinary Conference on Impacts, Volcanism, and Mass Mortality. In: Sharpton, V.L., Ward, P.D. (Eds.), Geol. Soc. Am. Spec. Pap., 247, pp. 271–288.